Calculation of beams of positrons, neutrons, and protons associated with terrestrial gamma ray flashes

Christoph Köhn[1] and Ute Ebert[1,2]

[1] Center for Mathematics and Computer Science, Amsterdam, Netherlands, [2] Department of Applied Physics, Eindhoven University of Technology, Eindhoven, Netherlands

Abstract Positron beams have been observed by the Fermi satellite to be correlated with lightning leaders, and neutron emissions have been attributed to lightning and to laboratory sparks as well. Here we discuss the cross sections to be used for modeling these emissions, and we calculate the emissions of positrons, neutrons, and also protons from lightning leaders. Neutrons were first erroneously attributed to fusion reactions, but the photonuclear reaction responsible for neutrons should create protons as well. We predict them here; they have not been observed yet. In the paper, we first revisit the model for stepped lightning leaders of Xu, Celestin, and Pasko with updated cross sections, we analyze the spatial and energetic structure of the electron beam, and we calculate the spectrum of the generated gamma ray beam at 16 km altitude. Then we review the scattering processes of photons with emphasis on the processes above 5 MeV, in particular the photon energy losses in Compton scattering events and the generation of leptons and hadrons. We provide simple approximations for photon energy loss and lepton and hadron production for any photon with energy above 5 MeV passing through an arbitrary air layer. Finally, we launch a gamma ray beam with the earlier calculated spectrum of the negative stepped lightning leader from 16 km upward and calculate the production and energy of positrons, neutrons, and protons as well as the propagation of positrons.

1. Introduction

1.1. High-Energy Emissions From Thunderstorms

High-energy emissions from thunderstorms were first observed from satellites. It started in 1994 with the discovery of terrestrial gamma ray flashes (TGFs) by the BATSE (Burst and Transient Source Experiment) satellite [*Fishman et al.*, 1994]. The RHESSI (Reuven Ramaty High Energy Solar Spectroscopic Imager) satellite [*Smith et al.*, 2005] and the Fermi Gamma-ray Space Telescope [*Briggs et al.*, 2010] have confirmed the production of high-energy bursts in thunderclouds, extended the measurements, and found quantum energies of up to 40 MeV. The team of the AGILE (Astro-rivelatore Gamma a Immagini LEggero) satellite measured energies up to 100 MeV [*Marisaldi et al.*, 2010; *Tavani et al.*, 2011].

Hard radiation was also measured from lightning leaders approaching ground [*Moore et al.*, 2001; *Dwyer et al.*, 2005] and from laboratory discharges [*Nguyen et al.*, 2008; *Rahman et al.*, 2008; *March and Montanyà*, 2010; *Shao et al.*, 2011; *Kochkin et al.*, 2012, 2014] where high-energy electrons are created in the streamer-leader stage. It was soon understood that these energetic photons were generated by the Bremsstrahlung process when energetic electrons collide with air molecules [*Fishman et al.*, 1994; *Torii et al.*, 2004].

In 2008 also flashes of electrons were reported [*Dwyer et al.*, 2008] before in December 2009 NASA's Fermi satellite detected beams of positrons and electrons [*Briggs et al.*, 2011], already predicted by *Dwyer* [2003], following the geomagnetic field lines sufficiently high above the atmosphere. They are distinguished from gamma ray flashes by their dispersion and by their location as electrons and positrons follow the geomagnetic field lines. The production of positrons in a run-away electron avalanche was predicted by *Gurevich et al.* [2000].

Fleischer et al. [1974] were the first to measure neutron fluxes from man-made discharges. By extrapolating their measurements, they estimated that there could be $4 \cdot 10^8$ thermal neutrons and $7 \cdot 10^{10}$ neutrons with energies of approximately 2.45 MeV per lightning flash.

Recently, *Agafonov et al.* [2013] wrote that they had measured the production of neutrons with kinetic energies between 0.01 eV and 10 MeV in laboratory discharges. However, these experiments are performed

with 1 MV applied to a 1 m gap, and it is not clear how neutrons with kinetic energies of up to 10 MeV could be created in these experiments. There are two mechanisms suggested for neutron production in a discharge [*Babich*, 2007]: fusion processes involving deuterium [*Young et al.*, 1973] or photoproduction where a photon is absorbed by an air molecule which subsequently releases a neutron. *Babich* [2007] discussed these processes using the relevant cross sections and rate coefficients. He concluded that the first process cannot play a significant role; hence, if any neutrons are produced, they must be due to photonuclear processes.

Two different physical mechanisms are currently discussed for the production of a substantial population of electrons in the MeV range and for subsequent other high energy emissions like gamma rays, positrons, or hadrons from thunderstorms: either relativistic run-away electron avalanches with feedback triggered by high-energy cosmic particles [*Wilson*, 1925; *Dwyer*, 2003, 2012; *Babich et al.*, 2012; *Gurevich*, 1961; *Gurevich et al.*, 1992; *Gurevich and Karashtin*, 2013] or thermal electrons accelerated in strong electric fields at the tips of lightning leaders [*Carlson et al.*, 2010; *Celestin and Pasko*, 2011; *Xu et al.*, 2012a, 2012b]. In the present study, we investigate the second mechanism.

To accelerate electrons from eV to tens of MeV, they first have to get into the runaway regime where friction cannot counteract the acceleration of the electric field anymore, and then they have to "fall" through a potential difference of tens of MV. A candidate for such electric fields are the tips of negative lightning leaders. In laboratory experiments [*Les Renardières Group*, 1978; *Gallimberti et al.*, 2002], as well as in thunderstorms, negative leaders have been observed to move stepwise [*Winn et al.*, 2011; *Edens et al.*, 2014]. *Moore et al.* [2001] proposed that the production of photons with energies above 1 MeV could be correlated with leader stepping, and *Dwyer et al.* [2005] showed that there is indeed a correlation between the stepping process and the production of X-rays. *Carlson et al.* [2009, 2010] have calculated the correlation between lightning leaders and the production of terrestrial gamma ray flashes. For a given photon spectrum, *Celestin and Pasko* [2012] calculated the influence of Compton scattering on the time resolution of a TGF signal at satellite altitudes. *Xu et al.* [2012a] were the first to model the production of TGFs from a negative stepped lightning leader. They assume that the upward directed leader channel is stationary and equipotential at some moment during the stepping process. They calculate the electric field of the leader in a fixed ambient field using the method of moments [*Balanis*, 1989]; the curvature at the leader tip enhances the electric field such that electrons can be accelerated from sub-eV into the run-away regime. They use a three-dimensional Monte Carlo code to trace electrons and to simulate the production and motion of Bremsstrahlung photons in air. But so far, no Monte Carlo simulation has modeled the production of positrons, neutrons, and protons for a photon spectrum of a negative stepped lightning leader. The present work is devoted to this task. Especially, we investigate the energy loss of photons with energies above 5 MeV and take the positron motion into account.

1.2. Organization of the Paper

This paper is divided into two parts. In section 2 we describe how we model the production of Bremsstrahlung photons from a negative stepped lightning leader. Since we use fully quantum field theoretical cross sections, appropriate for small atomic numbers as for air molecules and for electron energies above 1 keV, our results differ from those of previous authors [*Xu et al.*, 2012a; *Lehtinen*, 2000] who used a simple product ansatz of the energy dependend quantum electrodynamical term and a non-quantummechanical term for the angular distribution. In section 3 we present the cross sections to produce positrons and hadrons by photons scattered at air molecules for energies above 10 MeV and analytic estimates for the energy loss of photons within a given air layer. As a test case, we consider the production of positrons and hadrons by a photon beam with the energy distribution determined in section 2.

In section 2.1 we briefly describe how we model a stationary leader and the electron motion in its electric field. We also list the collisions implemented in our code. In sections 2.2.1 and 2.2.2 we present the spatial distribution of electron populations with energies above or below 1 MeV and the energy and direction of photons. The result suggests a simple representation of the distribution of high-energy photons which then is used as a starting point for further simulations in section 3. In section 2.2.3 we compare the influence of the Bethe-Heitler cross section and the Lehtinen cross section for electron-nucleus Bremsstrahlung on the production of photons from a stepped lightning leader.

In section 3.1 we briefly introduce photon processes in air and the production of positrons and hadrons. We also give details on modeling the positron motion through air. We list all cross sections we use for the motion of photons and positrons and estimate the influence of the geomagnetic field for the motion of relativistic electrons or positrons. In section 3.2 we present a simple approximation on how a photon with energy above 5 MeV is dissipated and produces leptons and hadrons when passing through arbitrary air layers. In section 3.3 we take the photon spectrum calculated in section 2, use its part above 5 MeV as an initial condition and launch a photon beam with this spectrum from 16 km upward. We present the positron and hadron distribution produced by this photon beam. Finally, we show how the positron distributions evolve in time and how the beam widens.

We briefly summarize our results in section 4.

In Appendix A, we present the electric field of a negative stepped lightning leader modeled as a conductive ellipsoid.

2. Gamma Ray Production by a Negative Stepped Lightning Leader at 16 km Altitude

A simplified model for a negative lightning leader during stepping, its electron acceleration and the subsequent gamma ray emission was introduced by *Xu et al.* [2012a, 2012b]. In the present section, we use essentially the same model and parameters, but with different cross sections, in particular, for the Bremsstrahlung that converts electron energies into photon energies. As already argued in *Köhn and Ebert* [2014a] and *Köhn et al.* [2014], previous authors have mainly used the cross sections presently embedded in Geant4 [*Agostinelli et al.*, 2003]. However, research on cross sections and development of databases is an ongoing activity. For light elements like oxygen and nitrogen in the energy range from keV to GeV, different cross sections are required, as they are currently embedded or being embedded into the *COsmic Ray SImulations for KAscade (CORSIKA)* [2013] simulation code for cosmic particle showers, into *Electron Gamma Shower (EGS5)* [2005], or into the Canadian software tool to model radiation transport [*Electron Gamma Shower by the National Research Council Canada (EGSnrc)*, 2014].

In our recent Fast Track Communication in J. Phys. D [*Köhn et al.*, 2014], we concentrated on the importance of including electron-electron Bremsstrahlung and already gave some results on electron acceleration and photon production during leader stepping. However, we were lacking the space to describe the model in detail. These details, images of the evolution of the distribution of electrons in space and energy, and a comparison with spectra derived with different cross-sections by other authors are presented in this section. It forms the starting step for the calculation of positron and hadron generation in the next section.

2.1. Set Up of the Model
2.1.1. Stepped Lightning Leader

For the stepped lightning leader, we use the model of *Xu et al.* [2012a] with the same parameters. The leader is vertical, 4 km long, and has a tip radius of 1 cm. It is assumed to be equipotential and embedded in an external thundercloud electric field of 0.5 kV/cm, far from the leader. This model approximates the leader at the moment of stepping: the space stem has connected to the leader, and the full electric potential is now on the new leader tip. At this moment the leader tip "explodes" with ionization, similarly as described by *Sun et al.* [2013], creating an inception cloud [*Briels et al.*, 2008] and later a streamer corona. The field of the leader is tested by inserting 50 electrons with 0.1 eV energy on the symmetry axis 30 cm ahead of the leader tip, as in the work of Xu et al. We also follow the approach of *Xu et al.* [2012a] by not taking the space charge effects of the developing corona discharge into account, but only that of the stationary leader; this approximation will be justified in Figure 3 for the electrons with the highest energy. Therefore, the approximation of taking only the electrostatic leader field into account is reasonable, even if the inception cloud develops into a relativistic impact ionization front [*Luque*, 2014].

Rather than approximating the leader as a cylinder with semispherical caps as *Xu et al.* [2012a], we approximate it as an ellipsoid with a length of 4 km and a curvature radius of 1 cm at the tip. This has the advantage that we can calculate the electric field $\mathbf{E}(\mathbf{r})$ analytically, as summarized in Appendix A. Figure 1 shows the electric field strength in the vicinity of the leader tip. It shows that the ellipsoid is a reasonable approximation when comparing with Figure 1a of *Xu et al.* [2012a], and it illustrates the strong field
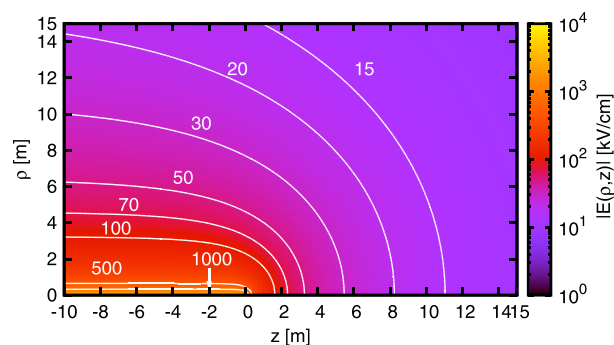
Figure 1. Electric field strength (color coded) in the vicinity of the tip for a leader of 4 km length in an ambient field of 0.5 kV/cm. Cylindrical coordinates ($\varrho = \sqrt{x^2 + y^2}, z$) are used, and the upper leader tip lies at the origin of the coordinate system. The white level lines indicate fixed values of the electric field strength from 15 to 1000 kV/cm as indicated.

enhancement close to the leader and its tip. The field is approximately 500 kV/cm at 30 cm ahead of the leader tip, thus certainly large enough to accelerate the electrons into the run-away regime.

2.1.2. Air Composition and Monte Carlo Approach

We model the air as consisting of 78.12% N_2, 20.95% O_2, and 0.93% Ar. To control the air density as a function of altitude, we use the barometric formula with a scale height of 8.33 km. We assume the upper leader tip where the electrons are accelerated to lie at 16 km altitude which corresponds to an air density of 1/10 of the density at sea level if the temperature change with altitude is taken into account.

We trace the positions of electrons and photons in three dimensions with a Monte Carlo code where the neutral air molecules are treated as a random background with appropriate statistical weight. Between collisions, the electrons follow classical or relativistic trajectories within the given electric field, depending on their energy, while the photons move with the speed of light into the direction of emission. The collisions are treated with a Monte Carlo scheme.

We now list the collision types included.

2.1.3. Cross Sections for Electrons

Details on our Monte Carlo code and its validation can be found in *Köhn et al.* [2014] and *Köhn and Ebert* [2014b]. There we also describe which collisions we take into account and how we have implemented them into our code. We remark here that the choice of cross sections is essential for correct results as shown in Appendix C of *Köhn and Ebert* [2014b] and that there is continued research on the cross sections for the propagation and production of high-energy particles in the atmosphere. Of particular importance is the correct modeling of Bremsstrahlung that creates the X and gamma rays from the high-energy electrons.

2.1.4. Electron-Nucleus Bremsstrahlung

Electron-nucleus Bremsstrahlung is the process when a free electron scatters at a nucleus and emits a photon, electron-electron Bremsstrahlung is the same process where the electron scatters at another electron and emits a photon. As electron-electron Bremsstrahlung is frequently considered as negligible compared to electron-nucleus Bremsstrahlung, the general term Bremsstrahlung refers typically to electron-nucleus Bremsstrahlung.

Different cross-sections for electron-nucleus Bremsstrahlung are used in different databases and by different researchers. In the field of terrestrial gamma ray flashes, *Carlson et al.* [2010] use the Geant4 simulation tool kit with its intrinsic cross sections [*Agostinelli et al.*, 2003]. *Dwyer* [2007] uses the Bethe-Heitler cross section [*Bethe and Heitler*, 1934; *Heitler*, 1944] resolving the full geometry of the process; he includes an atomic form factor to take the structure of the atomic shell into account. *Xu et al.* [2012a] use the simple product ansatz of *Lehtinen* [2000] to relate the energy and the direction of the emitted photons.

Now Geant4 [*Agostinelli et al.*, 2003] uses cross sections appropriate for the large atomic numbers Z of heavy nuclei while nitrogen and oxygen have $Z = 7$ and 8; thus, the cross sections implemented in Geant4 are not appropriate to simulate the production of Bremsstrahlung photons in air. According to *Shaffer et al.* [1996], the old Bethe-Heitler theory keeps being the appropriate theory for $Z < 29$ for electron energies between 1 keV and 1 GeV, hence for the production of TGFs, as we have already discussed in *Köhn and Ebert* [2014a]. In Appendix F of *Köhn and Ebert* [2014a] we have also shown that the atomic form factor used by *Dwyer* [2007] is close to unity in the relevant cases and thus negligible. The product ansatz of *Lehtinen* [2000] that is used by *Xu et al.* [2012a] is not compatible with the full quantum field theoretical treatment of collisions where the photon obtains almost all the electron energy, as we have discussed in Appendix E
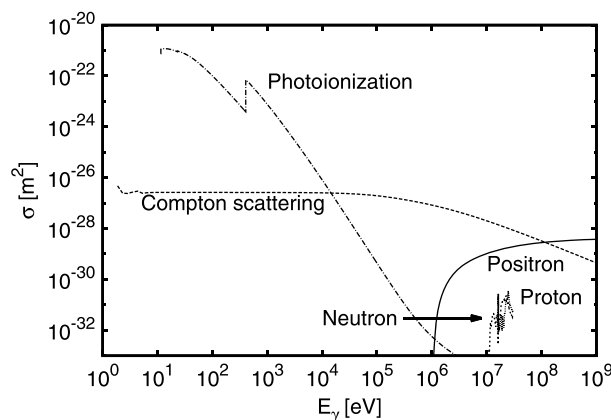
Figure 2. Total cross sections of photons for photoionization, Compton scattering, hadron production, and pair production as a function of incident photon energy E_γ for nitrogen.

of *Köhn and Ebert* [2014a]; we will compare results of TGF calculations under the same conditions using either the cross sections of *Lehtinen* [2000] or of *Köhn and Ebert* [2014a] in section 2.2.3.

We use the doubly differential cross section derived by *Köhn and Ebert* [2014a] for the relation between the photon energy $E_\gamma = \hbar\omega$ and the angle Θ_i between the incident electron and the emitted photon. This cross section has been obtained by integrating the direction of the emitted electron out in the Bethe-Heitler cross sections, and it is implemented using rejection sampling as described in *Knuth* [1997]. The scattered electron keeps its initial direction.

2.1.5. Electron-Electron Bremsstrahlung

As databases like Geant 4 concentrate on the Bremsstrahlung for metals like iron ($Z = 26$) or lead ($Z = 82$), electron-electron Bremsstrahlung is considered as irrelevant, because it scales with Z rather than with Z^2. Furthermore, the photons emitted in electron-electron Bremsstrahlung by nitrogen or oxygen ($Z = 7, 8$) are negligible as well compared to electron-nucleus Bremsstrahlung. However, we have shown recently [*Köhn et al.*, 2014] that electron-electron Bremsstrahlung also ejects the shell electron on which the free electron is scattered and that these electrons have higher energies than those created by normal impact ionization [*Yong-Ki and Santos*, 2000]. Using the cross sections of *Tessier and Kawrakow* [2007], the effect is important in air for electron energies of several MeV. Electron-electron Bremsstrahlung hence largely increases the number of electrons with energies above 1 MeV, and it subsequently contributes substantially to the number of high-energy photons from a negative stepped lightning leader. We remark here that electron-electron Bremsstrahlung also has been included recently in simulation packets like *CORSIKA* [2013] and *EGS5* [2005] simulating extensive air showers, as well as in *EGSnrc* [2014] for medical applications, but not yet in Geant4 [*Agostinelli et al.*, 2003] to the best of our knowledge.

2.1.6. Cross Sections for Photons

Figure 2 shows cross sections of photon processes as a function of the photon energy. For the photons, we use the cross sections for photoionization (Evaluated Photon Interaction Data (EPDL) Database, Photon and Electron Interaction Data, 1997, http://www-nds.iaea.org/epdl97/), Compton scattering [*Greiner and Reinhardt*, 1995; *Peskin and Schroeder*, 1995], hadron production [*Fuller*, 1985], and pair production (Bethe-Heitler in the integrated form of *Köhn and Ebert* [2014a]). Figure 2 shows that photoionization is dominant for photon energies below 1 keV. Thus, new electrons are created not only by electron impact ionization and the electron-electron Bremsstrahlung process, but also by photoionization.

2.2. Simulation Results
2.2.1. Distribution of Electrons in Energy and Space

In *Köhn et al.* [2014], we have already presented the electron energy distribution ahead of the stepped lightning leader after 24 ns of evolution when either including or neglecting the electron-electron Bremsstrahlung. There, we have presented the electron energy distribution for different runs with different realizations of random numbers, and we have seen that the energy distribution is stable against different sets of random numbers already for 50 initial particles; hence, 50 initial electrons is already enough for good statistics. Due to the limited space of a Fast Track Communication, we could not present the buildup of the spatial distribution. Therefore, we present here in Figure 3 this evolution including electron-electron Bremsstrahlung when 50 test electrons are inserted 30 cm ahead of the leader tip. The leader is indicated in black. The spatial distributions of the electrons after 5 ns, 10 ns, 15 ns, and 20 ns are plotted; the continuous colors indicate the electron densities with energies below 1 MeV, the color lines the electron densities with energies above 1 MeV in the *xz* plane where a slice was evaluated in the *y* direction from −3 cm to 3 cm.

The figure shows that at all instances, the high-energy electrons are ahead of the lower energy electrons and more on axis. The reason is obviously that the high-energy electrons are accelerated continuously while
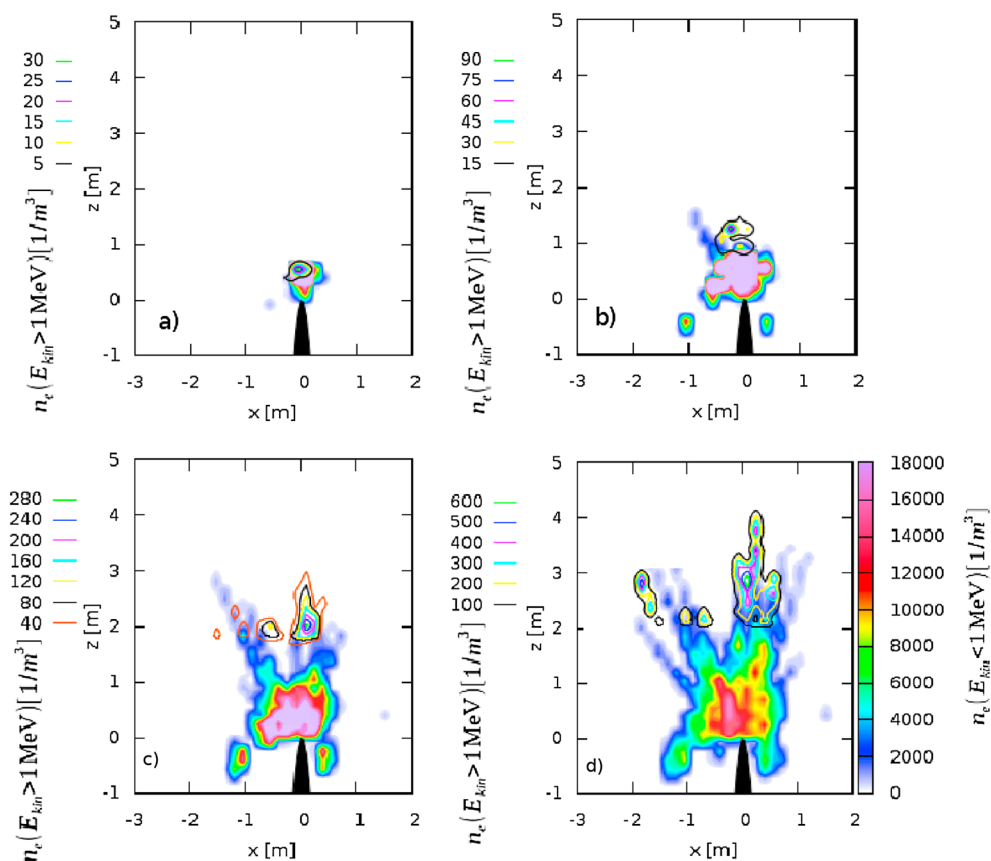
Figure 3. Evolution of the electron density distribution in the *xz* plane in a *y* range from −3 cm to 3 cm after (a) 5 ns, (b) 10 ns, (c) 15 ns, and (d) 20 ns. The bin size is $\Delta x = \Delta z = 16$ cm and $\Delta y = 6$ cm. The final moment $t = 24$ ns has already been displayed in Figure 2 in *Köhn et al.* [2014] with the same color scheme. The black ellipsoid indicates the position of the leader. Electrons with energies below or above 1 MeV are marked with different symbols. The density of electrons with energy below 1 MeV is indicated with continuous coloring, and the color map is the same in all panels. The density of electrons with energies above 1 MeV is indicated with color lines, and the values attributed to the color lines change for each panel.

the lower energy electrons have lost energy in collisions and these collisions also lead to a widening of the electron beam. The figure shows as well that new ionization patches are created at the sides of the leader, probably due to photoionization created by Bremsstrahlung photons. It should be noted though that the motion of the low-energy electrons is not quite physical as we neglect the space charge effects of the newly created ionization, just like *Xu et al.* [2012a, 2012b]. However, as there is a clear spatial separation between the electron populations at different energies, we argue that the calculation approximates the high-energy spectrum of the electrons well. We remark that electrons with energies of 10 keV, 100 keV, 1 MeV, and 10 MeV move with 19.5, 54.8, 94.1, and 99.9% of the speed of light and that light travels 6 m within 20 ns, while the fastest electrons are ≈ 4 m from the point of injection after 20 ns; see Figure 3d. The electrons with energies above 1 MeV are concentrated in one region on axis after 5 and 10 ns; after 15 ns, new patches with high-energy electrons have formed in new beam directions slightly off axis. We emphasize that the channel-like structures forming from 10 ns on are not streamers, as space charge effects are not included, but they are probably rather ionization traces of the created high-energy electrons, similarly as in cosmic particle showers [*Köhn and Ebert*, 2014b], but enhanced by the electric field.

We remark that the geomagnetic field has no influence on the electrons at these altitudes, and we will discuss the role of the geomagnetic field in more detail in section 3.

2.2.2. Distribution of Photons in Energy and Space

Figure 4 shows the photon energy distribution after 24 ns. As we have found in *Köhn et al.* [2014], the spectrum of Bremsstrahlung photons, and in particular the high energy tail, does not change considerably after about 15 ns. For reasons of computer memory, we anyhow have inserted only 50 test electrons into the
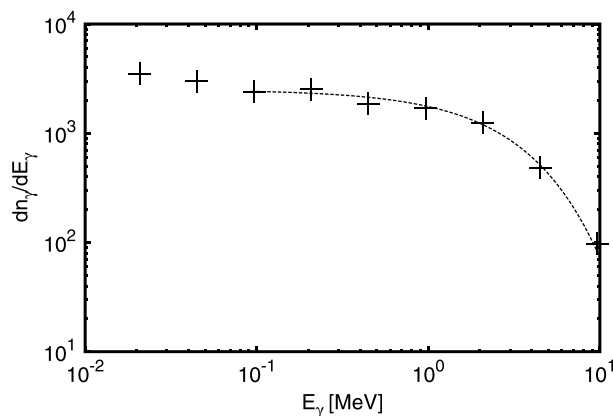
Figure 4. Photon energy distribution after 24 ns as calculated in *Köhn et al.* [2014]. The line shows the fit $\sim e^{-E_\gamma/3\text{MeV}}$.

leader field and we follow the motion of the electrons until 24 ns. The total number of photons with energies between 0.01 eV and 10 MeV in our simulation is approximately 5000; thus, there are 100 photons per initial electron. As we have neglected the space charge effects of the developing corona discharge, the low-energy part of the distribution is not quite physical and we concentrate here on photon energies above 10 keV. The maximal photon energy after 24 ns is approximately 10 MeV. Figure 4 also shows that for energies above 1 MeV, the distribution can be fitted well by the exponential $e^{-E_\gamma/3\text{ MeV}}$.

From our analysis in *Köhn and Ebert* [2014a], we know that photons with energies above 1 MeV are emitted predominantly in forward direction relative to the direction of the incident electron. Since the electrons, which can create such photons, mainly move upward (see Figure 3), this suggests to assume that the beam of initial photons is monodirectional. We will use this assumption in section 3.3 as a test case to simulate the production of positrons and hadrons.

2.2.3. Results for Different Bremsstrahlung Cross Sections
We tested the dependence of the simulation results on different Bremsstrahlung cross sections. Figure 5 shows the photon energy distribution after 24 ns for energies above 1 keV. The two curves are both without electron-electron Bremsstrahlung, and either the product ansatz of *Lehtinen* [2000] or the integrated Bethe-Heitler cross section of *Köhn and Ebert* [2014a] for the electron-nucleus Bremsstrahlung is used. The plot shows that the product ansatz of *Lehtinen* [2000] that is used by *Xu et al.* [2012a, 2012b] substantially overestimates the number of photons with energies above 20 keV, hence also the photons in the MeV range. We note here that there are some fluctuations due to the small number of produced photons; still the tendency of overestimating the number of high-energy photons is clearly observed.

3. Production and Motion of Positrons, Neutrons, and Protons in a TGF

In this section, we first discuss the elementary processes how photons convert their energy into leptons and hadrons and how positrons move through air, including the effect of the geomagnetic field on positrons and electrons. Then we present useful approximations for the production of positrons, neutrons, and protons for arbitrary gamma ray spectra in the energy range of 10 to 100 MeV within arbitrary air layers. Finally, we use the gamma ray spectrum derived in section 2 to calculate the production of positrons, neutrons, and protons and to follow the positron motion.

3.1. Elementary Photon Processes and Their Cross Sections
Figure 2 shows that the dominant mechanisms of photon scattering and photon energy loss change substantially for energies around 1 MeV. Photoionization is negligible, the creation of electron positron pairs starts to become important, and above about 10 MeV also neutrons and protons are generated. Also, Compton scattering changes its nature, as we will see below: the photons now mostly lose most of their energy rather than only a small fraction.
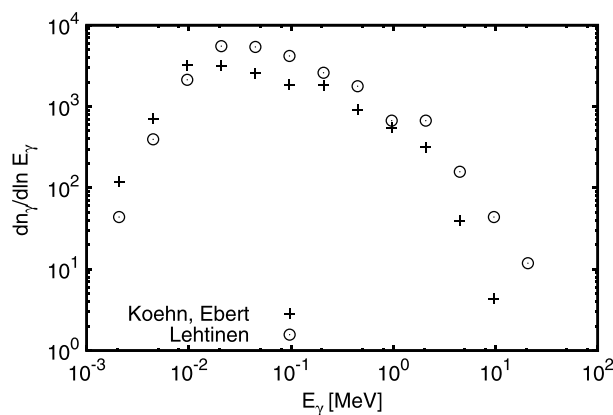

Figure 5. The photon energy distribution after 24 ns with: electron-nucleus Bremsstrahlung only, either according to *Köhn and Ebert* [2014a] (crosses) or according to *Lehtinen* [2000] (circles).
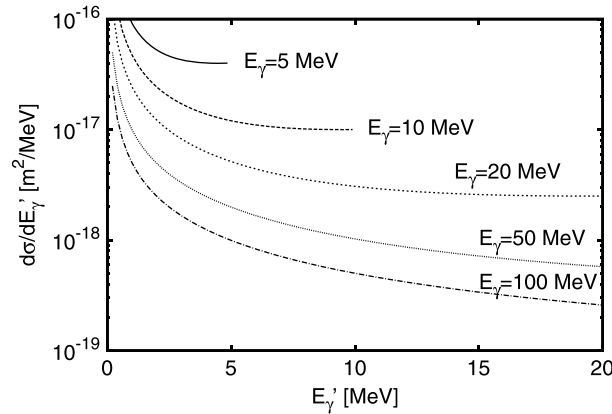
Figure 6. The differential cross section $\mathrm{d}\sigma/\mathrm{d}E'_\gamma$ of energies E'_γ of Compton scattered photons for different initial energies E_γ.

3.1.1. Compton Scattering

The cross section $\mathrm{d}\sigma/\mathrm{d}\Omega$ for Compton scattering is [*Greiner and Reinhardt*, 1995; *Peskin and Schroeder*, 1995]

$$\frac{\mathrm{d}\sigma}{\mathrm{d}\Omega} = \frac{\alpha^2 h^2}{2m^2 c^2} \frac{E'^2_\gamma}{E^2_\gamma} \left(\frac{E'_\gamma}{E_\gamma} + \frac{E_\gamma}{E'_\gamma} - \sin^2 \Theta \right) \tag{1}$$

where $\alpha \approx 1/137$ is the fine structure constant, $h \approx 6.6 \cdot 10^{-34}$ Planck's constant, $m \approx 9.1 \cdot 10^{-31}$ kg the electron mass, $c \approx 3 \cdot 10^8$ m/s the speed of light, and

$$E'_\gamma = \frac{E_\gamma}{1 + \frac{E_\gamma}{mc^2}(1 - \cos \Theta)} \tag{2}$$

is the energy of the scattered photon as a function of the incident photon energy E_γ and of the scattering angle Θ. Equation (2) can be solved as

$$\cos \Theta = 1 + \frac{mc^2}{E_\gamma} \left(1 - \frac{E_\gamma}{E'_\gamma} \right)$$

$$\Rightarrow \frac{\mathrm{d}\Omega}{\mathrm{d}E'_\gamma} = \frac{mc^2}{E'^2_\gamma}. \tag{3}$$

Thus, for the cross section $\mathrm{d}\sigma/\mathrm{d}E'_\gamma$ differential in the energy E'_γ one derives

$$\begin{aligned}
\frac{\mathrm{d}\sigma}{\mathrm{d}E'_\gamma} &= \frac{\mathrm{d}\sigma}{\mathrm{d}\Omega} \cdot \frac{\mathrm{d}\Omega}{\mathrm{d}E'_\gamma} \\
&= \frac{\alpha^2 h^2}{2m E^2_\gamma} \left[\frac{E'_\gamma}{E_\gamma} + \frac{E_\gamma}{E'_\gamma} - 1 + \left(1 + \frac{mc^2}{E_\gamma} \left(1 - \frac{E_\gamma}{E'_\gamma} \right) \right)^2 \right],
\end{aligned} \tag{4}$$

which is plotted in Figure 6. The figure shows that the largest part of the photon energy during Compton scattering is transferred onto electrons. Thus, the energy of photons is not shifted down slowly as in the energy range below 1 MeV [*Celestin and Pasko*, 2012]. As the number of new electrons produced through Compton scattering is small compared to the number of ambient electrons, we do not trace them in the rest of the section.

3.1.2. Generation of Hadrons

Photons also produce neutrons and protons in photonuclear reactions [*Fuller*, 1985] where a photon γ is absorbed by the nucleus of a molecule and a neutron n or a proton p is emitted:

$$^M_Z A + ^0_0\gamma \rightarrow ^{M-1}_Z A + ^1_0 n \tag{5}$$

$$^M_Z A + ^0_0\gamma \rightarrow ^{M-1}_{Z-1} B + ^1_1 p. \tag{6}$$

Here Z is the atomic number, and M is the rest mass of atom A; we note here that the emission of protons produces atoms B with atomic number $Z-1$ changing the composition of the ambient gas. In our model, we only use molecules of $^{14}_7$N and $^{16}_8$O as targets as the percentage of other nitrogen or oxygen isotopes in air is negligible. Since the binding energy E_{bind} of a nucleon is approximately 7.4 MeV for nitrogen and 8.0 MeV for oxygen (calculated with the Bethe Weizsäcker equation [*Weizsäcker*, 1935]), photons need tens of MeV to produce hadrons. The kinetic energy E_{kin} of the emitted hadron is

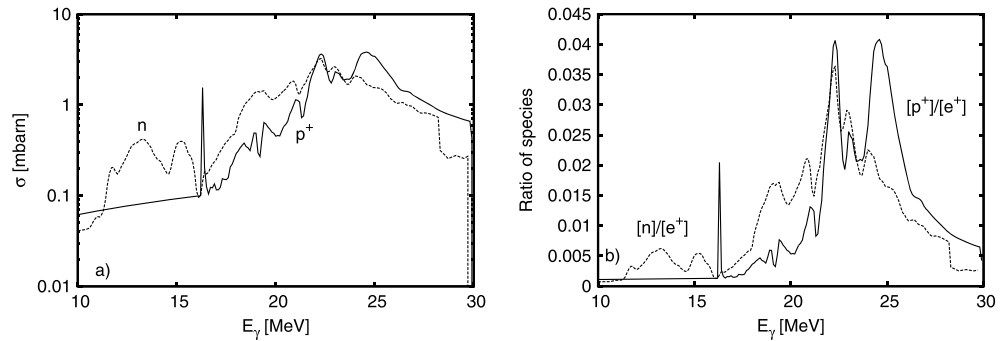$$E_{\mathrm{kin}} = E_\gamma - E_{\mathrm{bind}} \tag{7}$$

Figure 7. (a) The cross section for neutron (n) and proton (p^+) production of photons in air as a function of incident photon energy. (b) The ratio of neutron or proton production over positron production as a function of the incident photon energy.

if the nucleus is left behind in its ground state. Hadrons are emitted isotropically; we neglect the motion of the residual nuclei as their rest mass is much higher than the rest mass of a neutron or a proton.

Figure 7a shows the total cross section for the photoproduction of hadrons from air molecules. It shows that the photoproduction of hadrons is most efficient for photon energies between 20 MeV and 25 MeV. Figure 7b shows the ratio of the number of produced hadrons to the number of produced positrons; it shows that in this energy range, the production of hadrons is 1 to 2 orders of magnitude less than the production of positrons.

3.1.3. Production and Motion of Positrons

We sample the total positron energy E_+ and positron direction Θ_+ relative to the direction of the incident photon, using the differential cross section of Bethe and Heitler in the integrated form of *Köhn and Ebert* [2014a]. We use the same elastic scattering, ionization, and Bremsstrahlung cross sections as for electrons. This is feasible since cross sections for electrons and positrons are similar for kinetic energies above 1 MeV [*Agostinelli et al.*, 2003; *Kothari and Joshipura*, 2011]. We have also included the annihilation of positrons at shell electrons using analytic equations of *Greiner and Reinhardt* [1995]. Figure 8 shows the probability for annihilation of positrons at shell electrons of air molecules as a function of altitude for different positron energies when the positrons move from 16 km altitude upward excluding all other scattering processes. It shows that the probability is smaller than 15% for positron energies of 1 MeV and decreases rapidly with increasing positron energy.

3.1.4. Influence of the Geomagnetic Field

In order to estimate the influence of the geomagnetic field on relativistic electrons or positrons, we have to compare the gyration frequency in a magnetic field B with the collision fr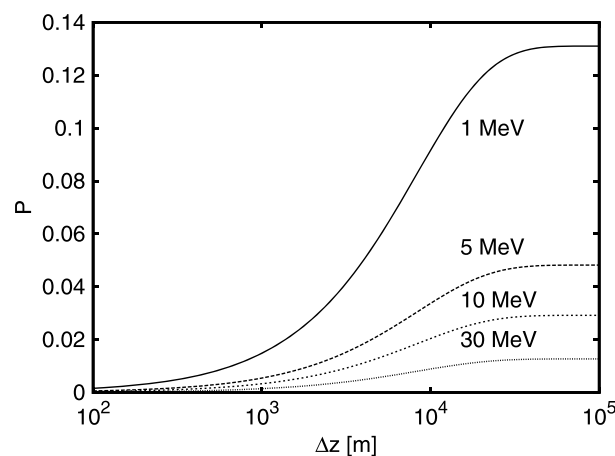equency of electrons. For energies below 1 keV, these frequencies were compared in *Ebert et al.* [2010]. In general, the gyration frequency ν_G is

Figure 8. The probability P of annihilation of positrons at shell electrons as a function of path length for different positron energies. Δz is the propagation distance of a positron moving straight upward from 16 km altitude.

$$\nu_G(E_{kin}) = \frac{1}{2\pi}\omega_G(E_{kin})$$
$$= \frac{1}{2\pi}\frac{e_0 B}{m(E_{kin})} = \frac{1}{2\pi}\frac{e_0 B c^2}{E_{kin}+m_0 c^2}$$
(8)

where we use the relativistic expression $m(E_{kin}) = (E_{kin}+m_0 c^2)/c^2$ for an electron with kinetic energy E_{kin} and e_0 and m_0 are the charge and the rest mass of an electron. The geomagnetic field is approximately $3 \cdot 10^{-5}$ T at the equator up to altitudes of approximately 300 km. Note that ν_G is not constant but decreases with increasing electron energy because of the energy dependence of the electron
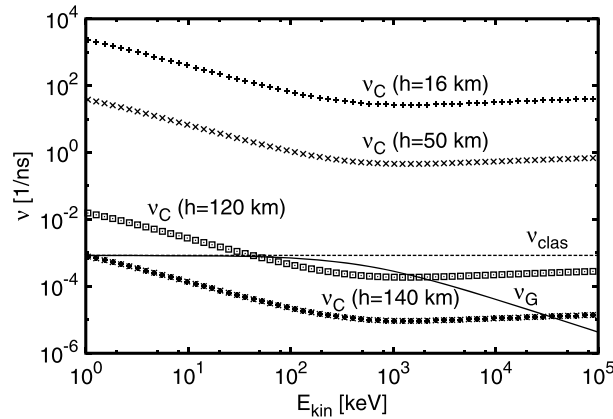
Figure 9. The gyration frequency ν_G (8) and the classical expression $\nu_{clas} = e_0 B/(2\pi \cdot m_0)$ for $B = 3 \cdot 10^{-5}$ T as well as the collision frequencies ν_C (9) at 16 km, 50 km, 120 km, and 140 km altitude as a function of the electron energy.

mass m. The classical approximation $\nu_{clas} = e_0 B/(2\pi \cdot m_0)$ where the electron mass is taken as constant is also plotted in Figure 9. It shows that the gyration frequency (8) starts to deviate from the classical value for energies above 10 keV; for 1 MeV the gyration frequency is only one quarter of the classical value. The collision frequency ν_C is

$$\nu_C = \sigma_{tot}(E_{kin}) n_B(z) v(E_{kin})$$
$$= \sigma_{tot}(E_{kin}) n_B(z) c \sqrt{1 - \frac{m_0^2 c^4}{(E_{kin} + m_0 c^2)^2}} \quad (9)$$

where $\sigma_{tot}(E_{kin})$ is the total cross section as a function of E_{kin}, and where $n_B(z)$ is the gas density as a function of altitude.

Figure 9 shows the comparison of the gyration frequency (8) and the collision frequency (9) for different altitudes for electron energies above 1 keV. It shows that for 16 km or 50 km and for energies between 1 keV and 100 MeV, the collision frequency is higher than the gyration frequency. Thus, the geomagnetic field is negligible. For approximately 120 km electrons with energies of $\approx$ 1 MeV start to feel the influence of the geomagnetic field. For approximately 140 km altitude the collision frequency is smaller than the gyration frequency for energies below 40 MeV. Hence, for altitudes between 120 km and 140 km, electrons and positrons with energies between 1 MeV and 40 MeV start to gyrate around the geomagnetic field lines. In our simulations we do not take the geomagnetic field into account. For altitudes below 120 km altitude and electron or positron energies above 1 MeV, we have just shown that the geomagnetic field is negligible; for altitudes substantially above 120 km beams of electrons and positrons follow the geomagnetic field lines, and their spatial distribution in the planes orthogonal to the field lines does not change any more.

3.2. Photon Energy Conversion Above 5 MeV for Arbitrary Spectra and Air Layers
The fact that photons above 5 MeV do not lose their energy continuously allows a very useful approximation that is not possible at lower energies. One can assume that the photons move straight until a collision process and that after the collision they can be removed from the list of photons with energies above 5 MeV. This holds for all three major loss processes: Compton scattering, pair production, and photonuclear hadron production. Figure 10 shows the cumulative total cross sections σ for these processes for photons with energies between 10 MeV and 100 MeV.

The column density of air between two points $\mathbf{r}_1$ and $\mathbf{r}_2$ is defined as

$$N_{int}(\mathbf{r}_1, \mathbf{r}_2) := \int_{\mathbf{r}_1}^{\mathbf{r}_2} d\ell \; n(\mathbf{r}), \quad (10)$$

where $d\ell$ parameterizes the straight line between these two points. A collision with cross section σ is likely if a photon has traveled through a column density larger than $1/\sigma$, i.e., if $\sigma \cdot N_{int} \gg 1$.

Figure 10 also includes the vertical column densities $N_{int}(16 \text{ km}, 20 \text{ km})$ and
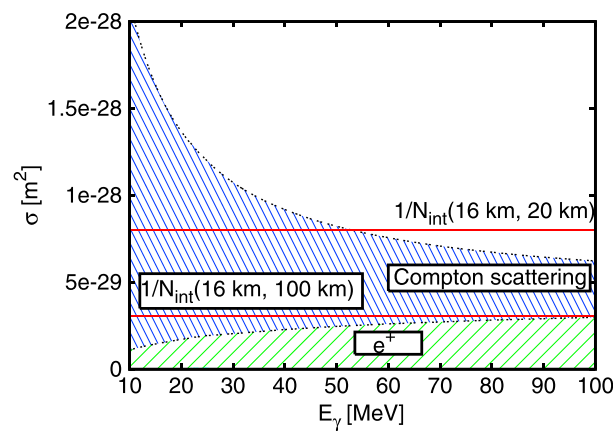

Figure 10. The cumulative cross sections as a function of the incident photon energy for positron production (green, wide hatches) and Compton scattering (blue, narrow hatches) in air. The red lines denote the inverse of the integrated air density from 16 km up to 20 km or up to 100 km, $N_{int}(a, b) = \int_a^b n(z) dz$.
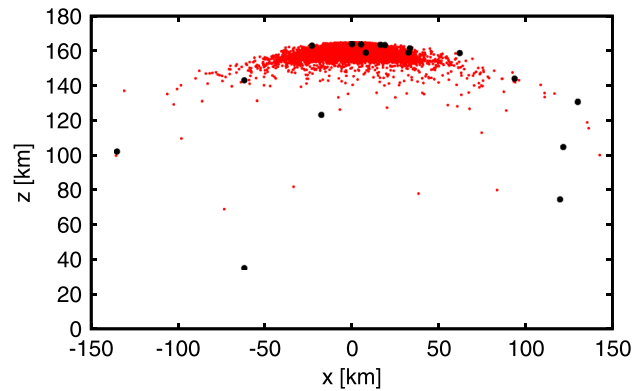
Figure 11. The positions of positrons (red dots) or photons with energies above 5 MeV (black dots) after 0.5 ms. Here the geomagnetic field is neglected. As discussed in section 3.1.4, it becomes important above about 120 km.

N_{int}(16 km, 100 km) in the atmosphere, using the atmospheric density profile $n(z) = 2.6885 \cdot 10^{25}$ 1/m^3 $e^{-z/8.33\ km}$. Hence, the figure shows that photons with energies between 10 MeV and 50 MeV are very likely to either create an electron-positron pair or a hadron or to lose most of their energy through Compton scattering in the air layer between 16 and 20 km altitude. Hence, only a small fraction of these high-energy photons will reach satellite altitudes, in agreement with Østgaard et al. [2008] and Gjesteland et al. [2010]. On the other hand, it is remarkable how the cumulative cross section decreases for higher photon energies. Hence, a photon with 100 MeV energy can cross the air layer from 16 to 100 km altitude with a probability of about one half according to the figure. Although this does not give any information about the production of photons with energies of approximately 100 MeV and thus cannot solely explain the spectra measured by AGILE, this might shed new light on the observation of 100 MeV photons at the AGILE satellite by Marisaldi et al. [2010].

Figure 10 shows as well, which fraction of the photons will create electron positron pairs, as this is simply the cross section of pair creation divided by the column density. The production of protons and neutrons relative to the positron production can be read from Figure 7b.

3.3. The Photon Spectrum of Section 2 as an Example
We now use the photon distribution at 16 km altitude as in Figure 4 as an example input to model the production of leptons and hadrons.

3.3.1. Initial Condition
The solid line in Figure 4 shows that the number n_γ of photons with energy E_γ can be fitted well with

$$n_\gamma(E_\gamma) \sim e^{-E_\gamma/3MeV} \tag{11}$$

for photon energies above 1 MeV.

As shown in Figure 2, pair production and hadron production become relevant for energies above approximately 10 MeV. Since measurements [Briggs et al., 2010; Marisaldi et al., 2010; Tavani et al., 2011] have shown that TGFs can have energies of up to 40 MeV, we use the distribution (11) in the energy range from 5 MeV to 40 MeV as an initial condition and populate it with approximately 1.2 million photons. As the photons in our simulation are produced within 24 ns, thus within some meters and without much spatial separation, we initiate the photon beam at one single point at 16 km altitude at time zero. We use a monodirectional beam because most high-energy electrons move in forward direction and because the photons with energies above several MeV are emitted in forward direction. We trace the photon beam and its particle production for 1 ms which corresponds to a distance of approximately 300 km, and we use the barometric formula for the air density as a function of altitude.

3.3.2. The Energy and the Temporal Evolution of Positrons and the Energy of Hadrons
The photon beam (11) propagates upward with the scattering processes described earlier, and we have calculated the position and energy of photons and positrons after 0.5 ms. Figure 11 shows the position of photons (black) with energies above 5 MeV and of positrons (red) after 0.5 ms. As explained in section 3.2, Figure 10 shows that a collision of a photon with an air molecule is very likely between 16 km and 20 km altitude. Thus, almost all photons have either disappeared due to the production of positrons or hadrons or lost so much energy through Compton scattering that their energy is less than 5 MeV and that they are removed from the pool of simulated photons. In contrast, Celestin and Pasko [2012] investigated photons with energies below 1 MeV where photons lose a smaller fraction of their energy through Compton scattering. Furthermore, Figure 11 shows that the positron beam moves with almost the speed of light.
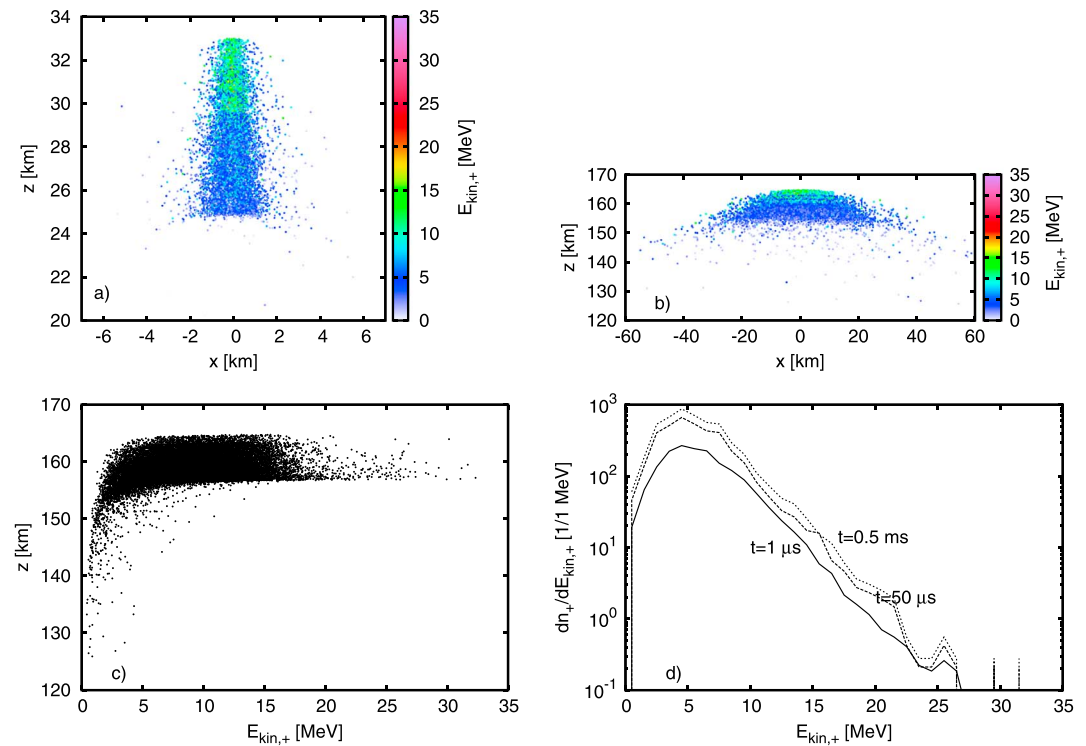
Figure 12. The spatial distribution of positrons after (a) 50 μs and (b) 0.5 ms. The color code resolves the kinetic energy. (c) The altitude as a function of the kinetic energy after 0.5 ms. (d) The energy distributions of positrons after 1 μs, 50 μs, and 0.5 ms. The original photon beam was ejected at 16 km altitude on the axis. As remarked in section 3.1.4 and in Figure 11, the geomagnetic field has been neglected.

Figure 12 shows the position and energies of all positrons including the positron scattering processes elastic scattering, ionization and Bremsstrahlung production. Figures 12a and 12b show the positron beam after 50 μs and 0.5 ms where the color denotes their kinetic energy. Figure 12c explicitly shows that positrons with energies above 20 MeV are in the front part of the positron beam while positrons with energies below 5 MeV are located rather at the end. Figure 12d shows the energy distribution of positrons after 1 μs, 50 μs, and 0.5 ms. It has a clear maximum at approximately 5 MeV. The shape of the distribution does not change considerably in time but only the total positron number.

Figure 13 shows the energy distributions of neutrons (Figure 13a) and protons (Figure 13b) after 10 μs, i.e., briefly after they have been produced, since we do not trace them through air. In both cases there are distinct maxima and minima due to the discrete structure of the photonuclear cross sections as shown in Figure 7. For neutrons the energies range from 4 MeV to 24 MeV; protons even have energies up to 33 MeV.
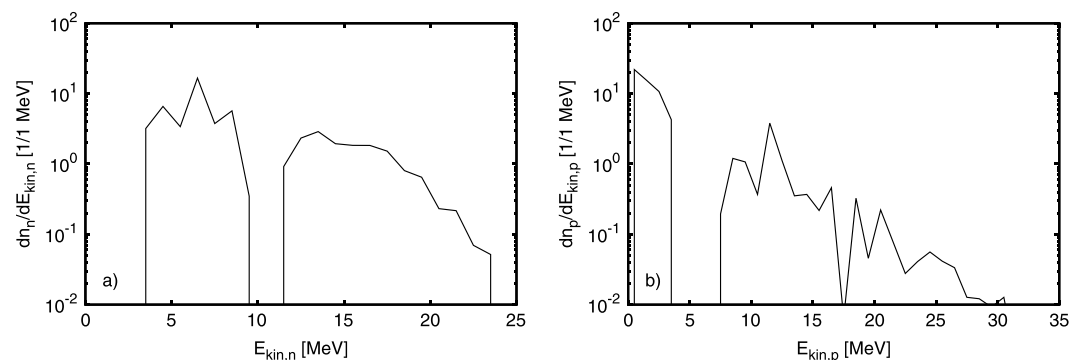

Figure 13. The energy distribution of (a) neutrons and (b) protons after 14 μs which corresponds to a photon travel distance of approximately 4 km.

Our calculations are consistent with results of *Babich* [2007] and extend it. *Babich* [2007] calculates photon and neutron fluxes from an upward propagating atmospheric discharge with the help of cross sections and rate coefficients. He determines the mean energies of neutrons to be approximately 10 MeV which is consistent with the energy distribution of neutrons in Figure 13. Proton generation, however, has not been predicted before.

4. Conclusion and Outlook

We have adopted the model of *Xu et al.* [2012a, 2012b], and we have simulated the acceleration of electrons and the production of Bremsstrahlung photons from a negative stepped lightning leader at 16 km altitude starting with 50 initial electrons. We have provided an analytical approximation for the electric field of a stationary leader in an ambient field. Using the electron-nucleus Bremsstrahlung cross section [*Köhn and Ebert*, 2014a] based on the Bethe-Heitler theory, appropriate for small atomic numbers Z and for electron energies above 1 keV, we have calculated the energy distribution of Bremsstrahlung photons and compared this distribution with the one calculated by *Xu et al.* [2012a] using different cross sections [*Lehtinen*, 2000]. We have seen that the cross sections of *Lehtinen* [2000] lead to unphysically high photon energies. Adding also electron-electron Bremsstrahlung [*Köhn et al.*, 2014], we have calculated the spatial distribution of electrons; some electrons reach the run-away regime and produce Bremsstrahlung photons with energies of up to 10 MeV. Photons with energies above 1 MeV are emitted forward relative to the direction of the incident electrons. In our simulations we obtain approximately 5000 photons with energies from 0.01 eV up to 10 MeV, hence 100 photons per initial electron.

We have provided approximations for photon absorption and lepton and hadron generation for photons of any energy between 5 and 100 MeV crossing through an arbitrary air layer, as illustrated in Figure 10. Accordingly, photons with energies above 5 MeV and below 50 MeV will most likely lose most of their energy within 4 km distance after being emitted upward at 16 km altitude. They will either disappear through the production of leptons or hadrons or lose most of their energy through Compton scattering. Thus, most photons with energies between 5 MeV and 50 MeV produced at 16 km altitude cannot reach satellite altitudes; this creates the Compton tail in the photon energy distribution as described by *Østgaard et al.* [2008] and *Gjesteland et al.* [2010] that is independent of the initial photon energy distribution. Photons with energies around 100 MeV, on the other hand, do have a probability of about one half to reach a satellite when generated at 16 km altitude and traveling upward.

Using the photon distribution of section 2 as a test case, we have calculated the motion of photons and the generation of positrons and hadrons. The positron distribution shows a maximum at 5 MeV and energies up to approximately 35 MeV. Most of the positrons are emitted in forward direction; a relativistic beam is formed moving with nearly the speed of light. Positrons with energies below 5 MeV can be found rather in the back of the beam. We have calculated the energy dissipation of positrons in air moving upward from 16 km altitude, and we have seen that the positron distribution does not change considerably in time.

We have shown that photons from a negative stepped lightning leader are also able to produce neutrons and protons. The energies of neutrons and protons range from 5 MeV up 33 MeV; *Babich* [2007] predicts mean energies of 10 MeV for neutrons by calculating neutron fluxes with rate coefficients and cross sections starting from a relativistic run-away electron avalanche. In contrast, we have taken a more realistic photon spectrum and more photon processes into account, and thus, we have obtained a more accurate energy spectrum of neutrons, and even of protons that have not been predicted or measured before.

In future work, a proper model for the motion of hadrons is developed which contains appropriate cross sections for the interaction of neutrons or protons with air molecules. Consequently, it will be possible to estimate the flux of hadrons upward and downward. This will be of interest to estimate how many hadrons will reach Earth's surface or satellites and hence can be measured.

Appendix A: The Electric Field of a Negative Leader

A1. Calculation of the Electric Field of a Negative Leader
Adopting the model of *Xu et al.* [2012a], we need to calculate the electric field of a stationary negative leader. We here calculate **E**(**r**) analytically assuming the leader be spheroidal; i.e., an ellipsoid of revolution with one long and two very short equal axes.

The spheroidal coordinates are defined by the solutions u of

$$\frac{x^2 + y^2}{b^2 + u} + \frac{z^2}{a^2 + u} = 1, \ a > b \tag{A1}$$

where $(0, 0, 0)$ is the center of the ellipsoid and the small half axis b is the same in x and y direction. The electric potential of a conducting ellipsoid in an ambient electric field E_0 in the z direction is [*Landau and Lifshitz*, 1963]

$$\Phi(\mathbf{r}) = -E_0 z \left[1 - \frac{\int_\xi^\infty \frac{ds}{(s+a^2)R_s}}{\int_0^\infty \frac{ds}{(s+a^2)R_s}} \right] \tag{A2}$$

with $R_s = \sqrt{(s + a^2)(s + b^2)}$ and

$$\xi(\mathbf{r}) = \frac{1}{2} \left[-a^2 - b^2 + z^2 + \varrho^2 + \sqrt{(-a^2 - b^2 + z^2 + \varrho^2)^2 + 4(-a^2 b^2 + b^2 z^2 + a^2 \varrho^2)} \right] \tag{A3}$$

as a solution of (A1) with $\varrho^2(x, y) := x^2 + y^2$, $\xi(\mathbf{r}) \geq -a^2$ and $\xi(\mathbf{r}) \equiv 0$ on the leader surface. The components of the electric field are

$$E_\varrho = -\frac{\partial \Phi}{\partial \varrho} = \frac{E_0 z}{\int_0^\infty \frac{ds}{(s+a^2)R_s}} \frac{1}{(\xi + a^2)R_\xi} \frac{\partial \xi}{\partial \varrho}, \tag{A4}$$

$$E_z = -\frac{\partial \Phi}{\partial z} = E_0 \left[1 - \frac{\int_\xi^\infty \frac{ds}{(s+a^2)R_s}}{\int_0^\infty \frac{ds}{(s+a^2)R_s}} \right] + \frac{E_0 z}{\int_0^\infty \frac{ds}{(s+a^2)R_s}} \frac{1}{(\xi + a^2)R_\xi} \frac{\partial \xi}{\partial z}. \tag{A5}$$

Furthermore

$$\nabla \xi(\mathbf{r}) = \mathbf{r} + \frac{\begin{pmatrix} x(a^2 - b^2 + z^2 + \varrho^2) \\ y(a^2 - b^2 + z^2 + \varrho^2) \\ z(-a^2 + b^2 + z^2 + \varrho^2) \end{pmatrix}}{\sqrt{(-a^2 - b^2 + z^2 + \varrho^2)^2 + 4(-a^2 b^2 + b^2 z^2 + a^2 \varrho^2)}} \tag{A6}$$

and

$$\int \frac{ds}{(s+a^2)R_s} = \frac{2}{(a^2 - b^2)\sqrt{s + a^2}} + \frac{1}{\sqrt{a^2 - b^2}^3} \ln \left(\frac{\sqrt{s + a^2} - \sqrt{a^2 - b^2}}{\sqrt{s + a^2} + \sqrt{a^2 - b^2}} \right) + C \tag{A7}$$

where C is an integration constant. By inserting (A6) and (A7) into (A4) and (A5), we obtain the electric field of a negative leader in the ambient field E_0:

$$\mathbf{E}(\mathbf{r}) = E_0 \left[1 - \frac{\frac{2\sqrt{a^2-b^2}}{\sqrt{\xi+a^2}} + \ln\left(\frac{\sqrt{\xi+a^2}-\sqrt{a^2-b^2}}{\sqrt{\xi+a^2}+\sqrt{a^2-b^2}}\right)}{\frac{2\sqrt{a^2-b^2}}{a} + \ln\left(\frac{a-\sqrt{a^2-b^2}}{a+\sqrt{a^2-b^2}}\right)} \right] \mathbf{e}_z$$

$$- \frac{E_0 z}{\sqrt{\xi + a^2}^3 (\xi + b^2)} \frac{1}{\frac{2}{(a^2-b^2)a} + \frac{1}{\sqrt{a^2-b^2}^3} \ln\left(\frac{a-\sqrt{a^2-b^2}}{a+\sqrt{a^2-b^2}}\right)}$$

$$\times \left[\mathbf{r} + \frac{\begin{pmatrix} x(a^2 - b^2 + z^2 + \varrho^2) \\ y(a^2 - b^2 + z^2 + \varrho^2) \\ z(-a^2 + b^2 + z^2 + \varrho^2) \end{pmatrix}}{\sqrt{(-a^2 - b^2 + z^2 + \varrho^2)^2 + 4(-a^2 b^2 + b^2 z^2 + a^2 \varrho^2)}} \right] \tag{A8}$$

A2. Field Enhancement Close to the Tip

To estimate the field close to the tip, we evaluate (A8) on the symmetry axis $x = y \equiv 0$ for $z = a + a_0$ where a_0 is the distance from the tip. Obviously, $E_x = E_y \equiv 0$ and

$$\frac{E_z}{E_0} = 1 - \frac{\frac{2\sqrt{a^2-b^2}}{a+a_0} + \ln\left(\frac{a+a_0-\sqrt{a^2-b^2}}{a+a_0+\sqrt{a^2-b^2}}\right)}{\frac{2\sqrt{a^2-b^2}}{a} + \ln\left(\frac{a-\sqrt{a^2-b^2}}{a+\sqrt{a^2-b^2}}\right)}$$
$$- \frac{2}{(a+a_0)\left((a+a_0)^2 - a^2 + b^2\right)} \frac{1}{\frac{2}{(a^2-b^2)a} + \frac{1}{\sqrt{a^2-b^2}^3}\ln\left(\frac{a-\sqrt{a^2-b^2}}{a+\sqrt{a^2-b^2}}\right)}. \tag{A9}$$

References

Agafonov, A. V., A. V. Bagulya, O. D. Dalkarov, M. A. Negodaev, A. V. Oginov, A. S. Rusetskiy, V. A. Ryabov, and K. V. Shpakov (2013), Observation of neutron bursts produced by laboratory high-voltage atmospheric discharge, *Phys. Rev. Lett.*, *111*, 115003, doi:10.1103/PhysRevLett.111.115003.

Agostinelli, S., J. Allison, K. Amako, J. Apostolakis, H. Araujo, P. Arce, M. Asai, D. Axen, S. Banerjee, and G. Barrand (2003), G4-a simulation toolkit, *Nucl. Instrum. Methods Phys. Res., Sect. A*, *506*, 250–303. [Avaialable at http://geant4.web.cern.ch/geant4/.]

Babich, L. P. (2007), Neutron generation mechanism correlated with lightning discharges, *Geomag. Aeron.*, *47*, 664–670.

Babich, L. P., E. I. Bochkov, J. R. Dwyer, and I. M. Kutsyk (2012), Numerical simulations of local thundercloud field enhancements caused by runaway avalanches seeded by cosmic rays and their role in lightning initiation, *J. Geophys. Res.*, *117*, A09316, doi:10.1029/2012JA017799.

Balanis, C. A. (1989), *Advanced Engineering Electromagnetics*, John Wiley, New York.

Bethe, H. A., and W. Heitler (1934), On the stopping of fast particles and on the creation of positive electrons, *Proc. Phys. Soc. London*, *146*, 83–112.

Briels, T. M. P., E. M. van Veldhuizen, and U. Ebert (2008), Time resolved measurements of streamer inception in air, *IEEE Trans. Plasma Sci.*, *36*, 908–909.

Briggs, M. S., et al. (2010), First results on terrestrial gamma ray flashes from the Fermi Gamma-ray Burst Monitor, *J. Geophys. Res.*, *115*, A07323, doi:10.1029/2009JA015242.

Briggs, M. S., et al. (2011), Electron-positron beams from terrestrial lightning observed with Fermi GBM, *Geophys. Res. Lett.*, *38*, L02808, doi:10.1029/2010GL046259.

Carlson, B., N. G. Lehtinen, and U. S. Inan (2009), Terrestrial gamma ray flash production by lightning current pulses, *J. Geophys. Res.*, *114*, A00E08, doi:10.1029/2009JA014531.

Carlson, B., N. G. Lehtinen, and U. S. Inan (2010), Terrestrial gamma ray flash production by active lightning leader channels, *J. Geophys. Res.*, *115*, A10324, doi:10.1029/2010JA015647.

Celestin, S., and V. P. Pasko (2011), Energy and fluxes of thermal runaway electrons produced by exponential growth of streamers during the stepping of lightning leaders and in transient luminous events, *J. Geophys. Res.*, *116*, A03315, doi:10.1029/2010JA016260.

Celestin, S., and V. P. Pasko (2012), Compton scattering effects on the duration of terrestrial gamma-ray flashes, *Geophys. Res. Lett.*, *39*, L02802, doi:10.1029/2011GL050342.

COsmic Ray SImulations for KAscade (CORSIKA) (2013), COsmic Ray SImulations for KAscade, Karlsruher Institut für Technologie, Karlsruhe, 19 Dec. 2014. [Available at http://www-ik.fzk.de/~corsika/.]

Dwyer, J. R. (2003), A fundamental limit on electric fields in air, *Geophys. Res. Lett.*, *30*(20), 2055, doi:10.1029/2003GL017781.

Dwyer, J. R. (2007), Relativistic breakdown in planetary atmospheres, *Phys. Plasmas*, *14*, 42901, doi:10.1063/1.2709652.

Dwyer, J. R. (2012), The relativistic feedback discharge model of terrestrial gamma-ray flashes, *J. Geophys. Res.*, *117*, A02308, doi:10.1029/2011JA017160.

Dwyer, J. R., et al. (2005), X-ray bursts associated with leader steps in cloud-to-ground lightning, *Geophys. Res. Lett.*, *32*, L01803, doi:10.1029/2004GL021782.

Dwyer, J. R., B. W. Grefenstette, and D. M. Smith (2008), High-energy electron beams launched into space by thunderstorms, *Geophys. Res. Lett.*, *35*, L02815, doi:10.1029/2007GL032430.

Ebert, U., S. Nijdam, C. Li, A. Luque, T. Briels, and E. van Veldhuizen (2010), Review of recent results on streamer discharges and discussion of their relevance for sprites and lightning, *J. Geophys. Res.*, *115*, A00E43, doi:10.1029/2009JA014867.

Edens, H. E., K. B. Eack, W. Rison, and S. J. Hunyady (2014), Photographic observations of streamers and steps in a cloud-to-air negative leader, *Geophys. Res. Lett.*, *41*, 1336–1342, doi:10.1002/2013GL059180.

Electron Gamma Shower (EGS5) (2005), Electron Gamma Shower, Stanford Univ., Stanford, Calif., 12 Feb. 2010. [Available at http://rcwww.kek.jp/research/egs/egs5.html.]

Electron Gamma Shower by the National Research Council Canada (EGSnrc) (2014), Electron Gamma Shower by the National Research Council Canada, Ottawa, 31 March 2013. [Available at http://www.nrc-cnrc.gc.ca/eng/solutions/advisory/egsnrc_index.html.]

Fishman, G. J., et al. (1994), Discovery of intense gamma-ray flashes of atmospheric origin, *Science*, *264*, 1313–1316.

Fleischer, R. L., J. A. Plumer, and K. Crouch (1974), Are neutrons generated by lightning?, *J. Geophys. Res.*, *79*, 5013–5017.

Fuller, E. G. (1985), Photonuclear reaction cross sections for ^{12}C, ^{14}N and ^{16}O, *Phys. Rep.*, *127*, 185–231.

Gallimberti, I., G. Bacchiega, A. Bondiou-Clergerie, and P. Lalande (2002), Fundamental processes in long air gap discharges, *C.R. Phys.*, *3*, 1335–1359.

Gjesteland, T., N. Østgaard, P. H. Connell, J. Stadsnes, and G. J. Fishman (2010), Effects of dead time losses on terrestrial gamma ray flash measurements with the burst and transient source experiment, *J. Geophys. Res.*, *115*, A00E21, doi:10.1029/2009JA014578.

Greiner, W., and J. Reinhardt (1995), *Quantenelektrodynamik*, Verlag Harri Deutsch, Frankfurt am Main, Germany.

Gurevich, A. V. (1961), On the theory of runaway electrons, *Sov. Phys. JETP-USSR*, *12*, 904–912.

Gurevich, A. V., and A. N. Karashtin (2013), Runaway breakdown and hydrometeors in lightning initiation, *Phys. Rev. Lett.*, *110*, 185005.

Gurevich, A. V., G. Milikh, and R. Roussel-Dupré (1992), Runaway electron mechanism of air breakdown and preconditioning during a thunderstorm, *Phys. Lett. A*, *165*, 463–468.

Gurevich, A. V., H. C. Carlson, Y. V. Medvedev, and K. P. Zybin (2000), Generation of electron-positron pairs in runaway breakdown, *Phys. Lett. A*, *275*, 101–108.

Heitler, W. (1944), *The Quantum Theory of Radiation*, Oxford Univ. Press, Oxford, U. K.

Yong-Ki, K., and J. P. Santos (2000), Extension of the binary-encounter-dipole model to relativistic incident electrons, *Phys. Rev. A*, *62*, 052710.

Knuth, D. E. (1997), *The Art of Computer Programming. Vol. 2: Seminumerical Algorithms*, Addison-Wesley, Boston, Mass.

Kochkin, P. O., C. V. Nguyen, A. P. J. van Deursen, and U. Ebert (2012), Experimental study of hard x-rays emitted from metre-scale positive discharges in air, *J. Phys. D: Appl. Phys.*, *45*, 425202.

Kochkin, P. O., A. P. J. van Deursen, and U. Ebert (2014), Experimental study of the spatio-temporal development of metre-scale negative discharge in air, *J. Phys. D: Appl. Phys.*, *47*, 145203.

Köhn, C., and U. Ebert (2014a), Angular distribution of Bremsstrahlung photons and of positrons for calculations of terrestrial gamma-ray flashes and positron beams, *Atmos. Res.*, *135–136*, 432–465.

Köhn, C., and U. Ebert (2014b), The structure of ionization showers in air generated by electrons with 1 MeV energy or less, *Plasma Sources Sci. Technol.*, *23*, 045001.

Köhn, C., U. Ebert, and A. Mangiarotti (2014), The importance of electron-electron Bremsstrahlung for terrestrial gamma-ray flashes, electron beams and electron-positron beams, *J. Phys. D: Appl. Phys.*, *47*, 252001.

Kothari, H. N., and K. N. Joshipura (2011), Total and ionization cross-sections of N_2 and CO by positron impact: Theoretical investigations, *Pramana - J. Phys.*, *76*, 477–488.

Landau, L. D., and E. M. Lifshitz (1963), *Electrodynamics of Continuous Media*, Pergamon Press, Oxford, U. K.

Lehtinen, N. G. (2000), Relativistic runaway electrons above thunderstorms, PhD thesis, Stanford, Calif.

Les Renardières Group (1978), Negative discharges in long air gaps at les Renardières, Paper presented at the request of the Chairman of Study Committee No 33.

Luque, A. (2014), Relativistic runaway ionization fronts, *Phys. Rev. Lett.*, *112*, 045003.

March, V., and J. Montanyà (2010), Influence of the voltage-time derivative in X-ray emission from laboratory sparks, *Geophys. Res. Lett.*, *37*, L19801, doi:10.1029/2010GL044543.

Marisaldi, M., et al. (2010), Detection of terrestrial gamma ray flashes up to 40 MeV by the AGILE satellite, *J. Geophys. Res.*, *115*, A00E13, doi:10.1029/2009JA014502.

Moore, C. B., K. B. Eack, G. D. Aulich, and W. Rison (2001), Energetic radiation associated with lightning stepped-leaders, *Geophys. Res. Lett.*, *28*, 2141–2144.

Nguyen, C. V., A. P. J. van Deursen, and U. Ebert (2008), Multiple X-ray bursts from long discharges in air, *J. Phys. D Appl. Phys.*, *41*, 234012.

Østgaard, N., T. Gjesteland, J. Stadsnes, P. H. Connell, and B. Carlson (2008), Production altitude and time delays of the terrestrial gamma flashes: Revisiting the Burst and Transient Source Experiment spectra, *J. Geophys. Res.*, *113*, A02307, doi:10.1029/2007JA012618.

Peskin, M. E., and D. V. Schroeder (1995), *An Introduction to Quantum Field Theory*, Westview Press, Boulder, Colo.

Rahman, M., V. Cooray, N. A. Ahmad, J. Nyberg, V. A. Rakov, and S. Sharma (2008), X-rays from 80 cm long sparks in air, *Geophys. Res. Lett.*, *35*, L06805, doi:10.1029/2007GL032678.

Shaffer, C. D., X. M. Tong, and R. H. Pratt (1996), Triply differential cross section and polarization correlations in electron Bremsstrahlung emission, *Phys. Rev. A*, *53*, 4158–4163.

Shao, T., C. Zhang, Z. Niu, P. Yan, V. F. Tarasenko, E. K. Baksht, A. G. Burahenko, and Y. V. Shut'ko (2011), Diffuse discharge, runaway electron and X-ray in atmospheric pressure air in a inhomogeneous electrical field in repetitive pulsed modes, *Appl. Phys.*, *98*, 021506.

Smith, D. M., L. I. Lopez, R. P. Lin, and C. P. Barrington-Leigh (2005), Terrestrial gamma-ray flashes observed up to 20 MeV, *Science*, *307*, 1085–1088.

Sun, A. B., J. Teunissen, and U. Ebert (2013), Why isolated streamer discharges hardly exist above the breakdown field in atmospheric air, *Geophys. Res. Lett.*, *40*, 2417–2422, doi:10.1002/grl.50457.

Tavani, M., et al. (2011), Terrestrial gamma-ray flashes as powerful particle accelerators, *Phys. Rev. Lett.*, *106*, 018501.

Tessier, F., and I. Kawrakow (2007), Calculation of the electron-electron bremsstrahlung cross-section in the field of atomic electrons, *Nucl. Instrum. Methods Phys. Res., Sect. B*, *266*, 625–634.

Torii, T., T. Nishijima, Z. I. Kawasaki, and T. Sugita (2004), Downward emission of runaway electrons and bremsstrahlung photons in thunderstorm electric fields, *Geophys. Res. Lett.*, *31*, L05113, doi:10.1029/2003GL019067.

Weizsäcker, C. F. (1935), Zur Theorie der Kernmassen, *Z. Angew. Phys.*, *96*, 431–458.

Wilson, C. (1925), The electric field of a thundercloud and some of its effects, *Proc. Phys. Soc. London A*, *37*, 32D–37D.

Winn, W. P., G. D. Aulich, S. J. Hunyady, K. B. Eack, H. E. Edens, P. R. Krehbiel, W. Rison, and R. G. Sonnenfeld (2011), Lightning leader stepping, K changes, and other observations near an intracloud flash, *J. Geophys. Res.*, *116*, D23115, doi:10.1029/2011JD015998.

Xu, W., S. Celestin, and V. P. Pasko (2012a), Source altitudes of terrestrial gamma-ray flashes produced by lightning leaders, *Geophys. Res. Lett.*, *39*, L08801, doi:10.1029/2012GL051351.

Xu, W., S. Celestin, and V. P. Pasko (2012b), Terrestrial gamma ray flashes with energies up to 100 MeV produced by nonequilibrium acceleration of electrons in lightning, *J. Geophys. Res.*, *117*, A05315, doi:10.1029/2012JA017535.

Young, F. C., S . J. Stephanakis, and D. Mosher (1973), Neutron production by hot dense plasmas generated with high power pulsers, *IEEE Trans. Nucl. Sci.*, *20*, 439.